



Comments are due by: Comments deadline

Supporting internal notes

Correlations between jets and charged particles in Pb+Pb Collisions at 5.02 TeV:
<https://cds.cern.ch/record/2304504>

Measurement of angular and momentum distributions of charged particles within and around jets in Pb+Pb and pp collisions at $\sqrt{s_{NN}} = 5.02$ TeV with ATLAS at the LHC

Studies of the fragmentation of jets into charged particles in heavy-ion collisions can help in understanding the mechanism of jet quenching by the hot and dense QCD matter created in such collisions, the quark-gluon plasma. This paper presents a measurement of the angular distribution of charged particles around the jet axis in $\sqrt{s_{NN}} = 5.02$ TeV Pb+Pb and pp collisions, done using the ATLAS detector at the LHC. The measurement is performed for jets reconstructed with the anti- k_t algorithm with radius parameter $R = 0.4$, and is extended to a distance of $r = 0.8$ outside the jet cone. The charged particles in this analysis have transverse momenta in the 1 GeV - 63 GeV range while jets have a transverse momenta in the 126 GeV - 316 GeV range and are restricted to have an absolute value of the jet rapidity be less 1.7. Results are presented as a function of Pb+Pb collision centrality and distance from the jet axis for different jet and charged-particle transverse momenta ranges. There is an enhancement for charged particles with transverse momenta below 4 GeV in Pb+Pb collisions that increases for larger angular distances from the jet axis, while charged particles with transverse momenta above 4 GeV show a depletion. An enhancement of charged particles of all transverse momenta is also observed in the jet core.

Analysis Team

[*email:* atlas-ana-hion-2018-03-analysis-team@cern.ch]

Akshat Puri, Anne Sickles, Martin Rybar

Editorial Board

[*email:* atlas-ana-hion-2018-03-editorial-board@cern.ch]

Mario Martinez Perez(chair), Iwona Grabowska-Bold, Benjamin Nachman



Journal: Phys. Rev. C.

ATLAS Paper

ANA-HION-2018-03-PAPER

14th April 2019



Draft version 0.1

Measurement of angular and momentum distributions of charged particles within and around jets in Pb+Pb and pp collisions at $\sqrt{s_{\text{NN}}} = 5.02$ TeV with ATLAS at the LHC

The ATLAS Collaboration

Studies of the fragmentation of jets into charged particles in heavy-ion collisions can help in understanding the mechanism of jet quenching by the hot and dense QCD matter created in such collisions, the quark-gluon plasma. This paper presents a measurement of the angular distribution of charged particles around the jet axis in $\sqrt{s_{\text{NN}}} = 5.02$ TeV Pb+Pb and pp collisions, done using the ATLAS detector at the LHC. The measurement is performed for jets reconstructed with the anti- k_t algorithm with radius parameter $R = 0.4$, and is extended to a distance of $r = 0.8$ outside the jet cone. The charged particles in this analysis have transverse momenta in the 1 GeV - 63 GeV range while jets have a transverse momenta in the 126 GeV - 316 GeV range and are restricted to have an absolute value of the jet rapidity be less 1.7. Results are presented as a function of Pb+Pb collision centrality and distance from the jet axis for different jet and charged-particle transverse momenta ranges. There is an enhancement for charged particles with transverse momenta below 4 GeV in Pb+Pb collisions that increases for larger angular distances from the jet axis, while charged particles with transverse momenta above 4 GeV show a depletion. An enhancement of charged particles of all transverse momenta is also observed in the jet core.

Contents

1	Introduction	2
2	Experimental setup	3
3	Data sets and event selection	4
4	Jet and track selection	4
5	Analysis procedure	5
6	Systematic uncertainties	8
7	Results	10
8	Summary	18
	Appendix	20

1 Introduction

Ultra-relativistic nuclear collisions at the Large Hadron Collider (LHC) produce hot, dense matter called the quark-gluon plasma, QGP (see Refs. [1, 2] for recent reviews). Hard-scattering processes occurring in these collisions produce jets which traverse and interact with the QGP. The comparison between the rates and the characteristics of these jets when produced in heavy-ion or pp collisions provides information on the properties of the QGP.

Jets with large transverse momenta are observed to be produced in central lead-lead (Pb+Pb) collisions at the LHC at a rate that is reduced by a factor of two with respect to the expectation from these cross sections measured in pp interactions, re-scaled by the nuclear overlap function of Pb+Pb collisions [3–5]. Similarly, back-to-back dijet [6–8] and photon-jet pairs [9] are observed to have unbalanced transverse momenta in Pb+Pb collisions compared to pp collisions. These observations suggest that some of the energy from the hard-scattered parton is transferred outside of the jet through its interaction with the QGP.

Also of interest are measurements sensitive to the distributions of particles within the jet. Measurements of the jet shape [10] and the longitudinal fragmentation functions [11–13] were performed in 2.76 TeV Pb+Pb collisions. These measurements show an excess of both low and high momentum particles inside the jet compared to pp collisions. Particles carrying a large fraction of the jet momentum are generally closely aligned with the jet axis, whereas low momentum particles can have a much broader angular distribution extending outside the jet [14, 15]. Fragmentation function measurements have shown that particles with transverse momentum, p_T , less than 4 GeV are enhanced in Pb+Pb collisions compared to pp collisions [13]. These observations suggest that the energy lost by jets through the jet-quenching process is being transferred to soft particles within and around the jet [16, 17]. Measurements of yields of these particles as a function of transverse momentum and distance between the particle and the jet axis have a potential to constrain the models of jet energy loss processes in Pb+Pb collisions.

This note presents a measurement of charged particle p_T distributions inside and around jets. The measured yields are defined as¹:

$$D(p_T, r) = \frac{1}{N_{\text{jet}}} \frac{1}{A} \frac{dn_{\text{ch}}(p_T, r)}{dp_T}, \quad (1)$$

where N_{jet} is the number of jets in consideration, $A = \pi(r_{\text{max}}^2 - r_{\text{min}}^2)$ is the area of an annulus around the jet with its inner and outer radii r_{min} and r_{max} . The angular distance from the jet axis is given by $r = \sqrt{\Delta\eta^2 + \Delta\phi^2}$ ², and $n_{\text{ch}}(p_T, r)$ is the number of charged particles with a given p_T within the annulus. The ratios of the charged-particle yields measured in Pb+Pb and pp collisions,

$$R_{D(p_T, r)} = \frac{D(p_T, r)_{\text{Pb+Pb}}}{D(p_T, r)_{pp}} \quad (2)$$

allow evaluating the modifications between the two yields. The differences between the $D(p_T, r)$ distributions in Pb+Pb and pp are also shown and allow for quantifying the absolute differences between the Pb+Pb and pp systems even in regions where the $D(p_T, r)$ distributions in pp tend to 0.

$$\Delta D(p_T, r) = D(p_T, r)_{\text{Pb+Pb}} - D(p_T, r)_{pp} \quad (3)$$

The analysis is done using 0.49 nb⁻¹ of Pb+Pb collisions and 25 pb⁻¹ of pp collisions at center-of-mass energy of 5.02 TeV collected in 2015 by ATLAS. Jets are reconstructed with the anti- k_t algorithm [18] using a radius parameter $R = 0.4$ over a rapidity range of $|y^{\text{jet}}| < 1.7$. The measurement is presented for jets with transverse momenta (p_T^{jet}) in the 126 to 316 GeV range, for charged particles with $p_T > 1.0$ GeV and for the following successive intervals in r around the jet, forming the annuli with inner and outer radii r_{min} and r_{max} : 0.0, 0.05, 0.1, 0.15, 0.2, 0.25, 0.3, 0.4, 0.5, 0.6, 0.7, 0.8

2 Experimental setup

The measurements presented here are performed using the ATLAS calorimeter, inner detector, trigger, and data acquisition systems [19]. The calorimeter system consists of a sampling liquid-argon (LAr) electromagnetic (EM) calorimeter covering $|\eta| < 3.2$, a steel-scintillator sampling hadronic calorimeter covering $|\eta| < 1.7$, LAr hadronic calorimeters covering $1.5 < |\eta| < 3.2$, and two LAr forward calorimeters (FCal) covering $3.1 < |\eta| < 4.9$. The EM calorimeters are segmented longitudinally in shower depth into three layers with an additional pre-sampler layer. They have segmentation that varies with layer and pseudorapidity. The hadronic calorimeters have three sampling layers longitudinal in shower depth.

The inner detector measures charged particles within the pseudorapidity interval $|\eta| < 2.5$ using a combination of silicon pixel detectors, silicon microstrip detectors (SCT), and a straw-tube transition radiation tracker (TRT), all immersed in a 2 T axial magnetic field [19]. Each of the three detectors is

¹ ATLAS uses a right-handed coordinate system with its origin at the nominal interaction point (IP) in the center of the detector, and the z -axis along the beam pipe. The x -axis points from the IP to the center of the LHC ring, and the y -axis points upward. Cylindrical coordinates (r, ϕ) are used in the transverse plane, ϕ being the azimuthal angle around the z -axis. The pseudorapidity is defined in terms of the polar angle θ as $\eta = -\ln \tan(\theta/2)$. Transverse momentum and transverse energy are defined as $p_T = p \sin \theta$ and $E_T = E \sin \theta$, respectively. $\Delta R = \sqrt{(\Delta\eta)^2 + (\Delta\phi)^2}$ gives the angular distance between two objects with relative differences $\Delta\eta$ and $\Delta\phi$ in pseudorapidity and azimuth respectively.

² $\Delta\eta$ and $\Delta\phi$ are the distances between the jet axis and the charged particle position in pseudorapidity and azimuth.

composed of a barrel and two symmetric end-cap sections. The pixel detector is composed of four layers including the "insertable B-layer" (IBL) [20, 21]. The SCT barrel section contains four layers of modules with sensors on both sides, and each end-cap consists of nine layers of double-sided modules with radial strips. The TRT contains layers of staggered straws interleaved with fibers in the barrel and end-cap.

The zero-degree calorimeters (ZDCs) are located symmetrically at $z = \pm 140$ m and cover $|\eta| > 8.3$. The ZDCs use tungsten plates as absorbers, and quartz rods sandwiched between the tungsten plates as the active medium. In Pb+Pb collisions the ZDCs primarily measure "spectator" neutrons, that is neutrons that do not interact hadronically when the incident nuclei collide. A ZDC coincidence trigger is implemented by requiring the pulse height from both ZDCs to be above a threshold to accept the single-neutron peak.

A two-level trigger system is used to select the Pb+Pb and pp collisions. The first level is based on custom electronics while the second level, the High Level Trigger (HLT), is based on software. Minimum-bias (MB) events are recorded using trigger defined by a logical OR of following two triggers: 1) total energy Level-1 trigger; 2) veto on the total energy trigger and ZDC coincidence trigger at Level-1 with the additional requirement of least one track in the HLT. The total-energy trigger required a total transverse energy measured in the calorimeter system to be greater than 50 GeV. Jet events are selected by the HLT, seeded by a jet identified by the Level-1 jet trigger in pp collisions or by the total-energy trigger with a threshold of 50 GeV in Pb+Pb collisions. The Level-1 jet trigger utilized in pp collisions required a jet with transverse momentum greater than 20 GeV. The HLT jet trigger used a jet reconstruction procedure similar to that used in the offline analysis as discussed in Section 4. It selected events containing jets with the transverse energy of at least 75 GeV in Pb+Pb collisions and at least 85 GeV in pp collisions. The measurement is performed in the jet transverse momentum range where the trigger is fully efficient.

In addition to the jet-triggered sample, a separate Pb+Pb data sample that is used as the overlay in Pb+Pb Monte Carlo (MC) was recorded. This sample, referred to as "enhanced minimum-bias", was recorded with three trigger selections: the minimum-bias trigger and two total transverse-energy triggers with thresholds of 1.5 TeV and 6.5 TeV respectively, used to enhance the rate of central Pb+Pb events.

3 Data sets and event selection

The Pb+Pb and pp data used in this analysis were recorded in 2015. The data samples consist of 25 pb^{-1} of $\sqrt{s} = 5.02$ TeV pp data and 0.49 nb^{-1} of $\sqrt{s_{\text{NN}}} = 5.02$ TeV Pb+Pb data. The MB Pb+Pb sample was recorded with different pre-scales³ depending on the instantaneous luminosity in the LHC fill. The MB trigger recorded an effective luminosity of $22 \mu\text{b}^{-1}$. In Pb+Pb and pp collisions, events are required to have a reconstructed vertex within 150 mm of the nominal interaction point along the beam axis. Only events taken during stable beam conditions and satisfying detector and data-quality requirements that include the calorimeters and inner tracking detectors being in nominal operating conditions are considered.

A sample of 1.8×10^7 simulated 5.02 TeV POWHEG+PYTHIA8 [22, 23] pp hard-scattering events, generated using the A14 tune [24] and the NNPDF23LO PDF set [25], is used to evaluate the performance for measuring $D(p_T, r)$ distributions in the pp data. The performance of the detector and analysis procedure in Pb+Pb collisions is evaluated using 1.8×10^7 5.02 TeV hard-scattering dijet events generated with POWHEG+PYTHIA8 overlaid on top of events from the enhanced minimum-bias Pb+Pb data sample. In both samples, the detector response is simulated using GEANT4 [26, 27].

³ The pre-scale indicates which fraction of events that passed the trigger selection was selected for recording by the data acquisition.

In Pb+Pb collisions, the event centrality reflects the overlap area of the two colliding nuclei and is characterized by ΣE_T^{FCal} , the total transverse energy deposited in the FCal [28]. The six centrality intervals used in this analysis are defined according to successive percentiles of the ΣE_T^{FCal} distribution obtained in minimum-bias collisions, ordered from the most central (highest ΣE_T^{FCal}) to the most peripheral (lowest ΣE_T^{FCal}) collisions: 0–10%, 10–20%, 20–30%, 30–40%, 40–60%, 60–80%. A weight is assigned to each MC event such that the event sample obtained from the simulation has the same ΣE_T^{FCal} distribution as in data.

4 Jet and track selection

The jet reconstruction procedures closely follow those used by ATLAS for jet measurements in pp and Pb+Pb collisions at $\sqrt{s_{\text{NN}}} = 2.76$ TeV [4]. The anti- k_t algorithm is first run in four-momentum recombination mode, on $\Delta\eta \times \Delta\phi = 0.1 \times 0.1$ calorimeter towers with two anti- k_t distance parameter values ($R = 0.2$ and $R = 0.4$). The energies in the towers are obtained by summing the energies of calorimeter cells at the electromagnetic energy scale within the tower boundaries. Then, an iterative procedure is used to estimate the η -dependent underlying event (UE) transverse energy density, while excluding the regions populated by jets. The estimate of the UE contribution is performed on an event-by-event basis. Furthermore, the background is modulated to account for the presence of the azimuthal anisotropy of particle production [29]. The modulation accounts for the contribution of the second, third, and fourth order azimuthal anisotropy harmonics. Higher order harmonics introduce a negligible variation of the reconstructed jet energy. The UE transverse energy is subtracted from calorimeter towers included in the jet and the four-momentum of the jet is updated accordingly. Then, a jet η - and p_T -dependent correction factor to the p_T^{jet} derived from the simulation samples is applied to correct for the calorimeter energy response [30]. The same calibration factors are applied both in pp and Pb+Pb collisions. An additional correction based on *in-situ* studies of jets recoiling against photons, Z bosons, and jets in other regions of the calorimeter is applied [31, 32]. The same jet reconstruction procedure without the azimuthal modulation of the UE is also applied to pp collisions. In this analysis, jets are required to have p_T^{jet} in the 126–316 GeV range, with rapidity $|\eta^{\text{jet}}| < 1.7$. To prevent nearby jets from distorting the measurement of $D(p_T, r)$ distributions, jets are rejected if there is another jet with a higher p_T^{jet} than the considered jet anywhere within a distance of $\Delta R < 1.0$. The isolation requirement removes approximately 0.01% of jets, and has almost no impact on the final measurement.

Charged-particle tracks are reconstructed from hits in the inner detector using the track reconstruction algorithm with settings optimized for the high hit density in heavy-ion collisions [33]. Tracks used in this analysis are required to have at least 9 (11) total silicon hits for charged particles with pseudorapidity, $|\eta^{\text{ch}}| \leq 1.65$ ($|\eta^{\text{ch}}| > 1.65$). At least one hit is required in one of the two innermost pixel layers. If the track trajectory passes through an active module in the innermost layer, then a hit in this layer is required. Additionally, a track must have no more than two holes in the pixel and SCT detectors together, where a hole is defined by the absence of a hit predicted by the track trajectory. All charged-particle tracks used in this analysis are required to have reconstructed transverse momentum $p_T^{\text{ch}} > 1.6$ GeV. In order to suppress a contribution from secondary particles, the distance of closest approach of the track to the primary vertex is required to be less than a value which varies from 0.45 mm at $p_T^{\text{ch}} = 4$ GeV to 0.2 mm at $p_T^{\text{ch}} = 20$ GeV in the transverse plane and less than 1.0 mm in the longitudinal direction.

The efficiency, $\varepsilon(p_T^{\text{truth}}, \eta^{\text{truth}})$, for reconstructing charged particles in Pb+Pb and pp collisions is evaluated as a function of the generator-level primary particle transverse momentum, p_T^{truth} , and pseudorapidity,

η^{truth} by matching tracks to generator-level primary particles⁴ using the MC samples described above [27]. For Pb+Pb collisions, the efficiency is also evaluated separately in each centrality interval used in the measurement.

The contribution of reconstructed tracks that cannot be matched to a generated primary particle in the pp MC samples, along with the residual contribution of tracks matched to secondary particles, are together called the contribution from “fake” tracks. This contribution is less than 2% in the entire p_T^{ch} range under study in both pp and Pb+Pb collisions.

5 Analysis procedure

Reconstructed tracks are associated with a reconstructed jet if they fall within $\Delta R < 0.8$ of the jet axis. The measured track yields, $d^2n_{\text{ch}}^{\text{meas}}/dp_T^{\text{ch}}dr$ are constructed as:

$$\frac{d^2n_{\text{ch}}^{\text{meas}}}{dp_T^{\text{ch}}dr} = \frac{1}{\varepsilon(p_T^{\text{ch}}, \eta^{\text{ch}})} \frac{\Delta N_{\text{ch}}(p_T^{\text{ch}}, p_T^{\text{jet}}, r)}{\Delta p_T^{\text{ch}} \Delta r} \quad (4)$$

where $\Delta N_{\text{ch}}(p_T^{\text{ch}}, r)$ represents the number of associated tracks within a given p_T^{ch} and r range. The efficiency correction is applied as a $1/\varepsilon(p_T^{\text{ch}}, \eta^{\text{ch}})$ weight on a track-by-track basis, assuming $p_T^{\text{ch}} = p_T^{\text{truth}}$. While that assumption is not strictly valid, the efficiency varies sufficiently slowly with p_T^{truth} that the error introduced by this assumption is less than 1%. The efficiency increases from about 80% at $p_T = 1.0$ GeV to about 90% at $p_T = 10$ GeV, and remains constant thereafter. There is little dependence ($< 3\%$) on p_T^{jet} for the charged-particle transverse momentum range under investigation. In Pb+Pb collisions, the centrality dependence to the efficiency is also at the level of 3%.

The measured track yields in pp and Pb+Pb collisions need to be corrected for the presence of fake tracks and contributions from charged particles from the UE in Pb+Pb collisions. The UE contribution is evaluated as a function of p_T^{ch} , p_T^{jet} , r , azimuthal distance to the second order reaction plane angle (Ψ_2) [29], and the collision centrality. The UE charged-particle yields $dn_{\text{ch}}^{\text{UE}}/dp_T^{\text{ch}}$, are evaluated over $1.0 < p_T^{\text{ch}} < 10$ GeV. MC studies show that the UE contribution is negligible for charged particles with $p_T^{\text{ch}} > 10$ GeV.

The UE contribution is estimated using the Pb+Pb MC overlay events where the efficiency corrected differential yields of charged particles without a truth match, $dN_{\text{ch}}^4/d\phi d\eta dp_T^{\text{ch}} d\Psi_2$ are evaluated separately for each centrality selection. Here $d\Psi_2$ denotes the azimuthal distance between the charged particle and the second-order reaction plane angle⁵. These yields are further used to estimate the average, area normalized yields of charged particles for the jet under study, $1/A(r) \times d^2n_{\text{ch}}^{\text{UE}}(r)/dp_T^{\text{ch}}dr|_{\text{cent}}$ (“cent” refers to centrality), where $A(r)$ is the area of the annulus at distance r . The jet η and ϕ positions, as well as the azimuthal distance of the jet to the second-order reaction plane angle are taken into account. The yields are independent of the angular distance r , decrease with the decreasing collision centrality, increasing p_T^{ch} , and increasing azimuthal distance to the second-order reaction plane. The difference in the

⁴ Primary particles are defined as particles with a mean lifetime $\tau > 0.3 \times 10^{-10}$ s either directly produced in pp interactions or from subsequent decays of particles with a shorter lifetime. All other particles are considered to be secondary.

⁵ The reaction plane angle Ψ is determined on an event-by-event basis by a standard method using the ϕ variation of transverse energy in the forward calorimeter

centrality distribution between overlay sample and the jet-triggered sample is accounted for by a reweighing procedure.

A second method to calculate the UE is used to provide a systematic uncertainty. This method uses a regular grid of 9 cones of size $R = 0.8$ covering the full inner detector region. Cones within a distance of $dR = 1.6$ to a reconstructed jet are excluded if $p_T^{\text{jet}} > 90$ GeV, or if they contain a track with $p_T > 10$ GeV. The resulting UE charged particle yields $dn_{\text{ch}}^{\text{UECone}}/dp_T^{\text{ch}}$ are evaluated over the 1 – 10 GeV range as a function of p_T , p_T^{jet} centrality, and r , and then averaged over all cones according to

$$\frac{dn_{\text{ch}}^{\text{UECone}}}{dp_T^{\text{ch}}} = \frac{1}{N_{\text{cones}}} \frac{1}{\varepsilon} \frac{\Delta N_{\text{ch}}^{\text{cone}}(p_T^{\text{ch}}, p_T^{\text{jet}}, \eta^{\text{jet}})}{\Delta p_T^{\text{ch}}} \quad (5)$$

Here N_{cones} is the number of background cones associated with a given jet with p_T^{jet} . $\Delta N_{\text{ch}}^{\text{cone}}$ is the number of charged particles summed across all background cones associated to the jet in question. The cone method estimates the UE yields only from events containing jets included in the analysis, ensuring that the background automatically had the correct distribution of centralities within a given centrality bin. The UE contribution as measured using the cone method in data needs three corrections:

Correction for η -dependence: This accounts for differences in the yields of UE particles at the position of the jet and at the position of the track for the random cone entering the UE estimate. The correction is derived using the η distribution of charged particles from MC overlay events.

Correction for flow: There is a correction applied to account for the difference in the azimuthal particle density due to elliptic flow. This correction is based on a parametrization of the p_T^{ch} and centrality dependence of previously measured elliptic flow coefficients, v_2 [34].

UE and JER correlation: The steeply falling jet spectra coupled with the smearing due to a finite jet energy resolution leads to a net migration of jets from lower p_T to higher p_T values, causing the underlying event underneath a jet to be larger than what is estimated. This is accounted for by correcting the measured underlying event in data by a ratio of the underlying event measured by the nominal method in MC (which by definition considers only tracks without a truth match) and the cone method in MC. The size of the correction is negligible for larger r values or low p_T^{ch} where the UE is the largest and increases with decreasing r values and increasing p_T^{ch} . It has only a small dependence on p_T^{jet} .

The measured distributions both in pp and Pb+Pb collisions are further corrected for the presence of fake tracks. The contribution from these tracks to the $D(p_T, r)$ distributions is estimated from the MC samples without MB interactions overlaid. The corrected UE distributions with the addition of the fake track contribution, $1/A(r) \times d^2\tilde{n}_{\text{ch}}^{\text{UE+fake}}(r)/dp_T^{\text{ch}}dr|_{\text{cent}}$, are then subtracted from the measured distributions.

Figure 1 shows the charged-particle distributions prior to the UE and fake track subtraction, $d^2n_{\text{ch}}^{\text{meas}}/dp_T^{\text{ch}}dr$, divided by the distributions after the subtraction, $d^2n_{\text{ch}}^{\text{sub}}/dp_T^{\text{ch}}dr$ as a function of r for different p_T^{ch} intervals and for six centrality selections, for jets in the 126–158 GeV p_T^{jet} range. The UE is the highest for 1.0 GeV charged particles at large values of r and in central collisions for p_T^{jet} between 126–158 GeV. It is rapidly decreasing towards more peripheral collisions, larger p_T^{ch} and smaller r . Furthermore, the ratio is slowly decreasing with increasing p_T^{jet} .

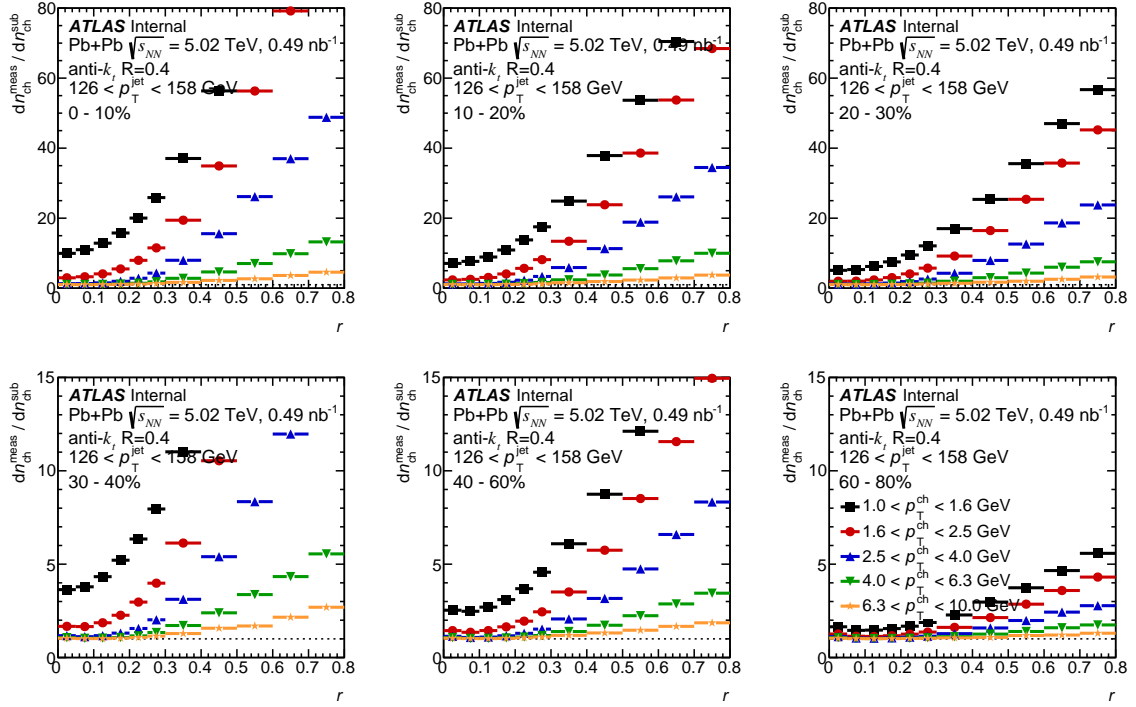


Figure 1: Ratio of the raw charged particle distributions to those after the subtraction of the UE and fake tracks as a function of r for different p_T^{ch} intervals, six centrality selections and for p_T^{jet} between 126–158 GeV.

To remove the effects of the bin migration due to the jet energy and track-momentum resolution, the subtracted $1/A(r) \times d^2 n_{\text{ch}}^{\text{sub}} / dp_T^{\text{ch}} dr$ distributions are corrected by a two-dimensional Bayesian unfolding [35] in p_T^{ch} and p_T^{jet} as implemented in the RooUnfold package [36]. Two-dimensional unfolding is used because the calorimetric jet energy response depends on the fragmentation pattern of the jet [37]. Four-dimensional response matrices are created from the MC samples using the generator-level and reconstructed p_T^{jet} , and the generator-level and reconstructed charged-particle p_T^{ch} . Separate unfolding matrices are constructed for the pp and Pb+Pb system. The Bayesian procedure requires a choice in the number of iterations. Additional iterations reduce the sensitivity to the choice of prior, but may amplify statistical fluctuations in the distributions. After four iterations the $D(p_T, r)$ distributions are found to be stable for both the Pb+Pb and pp data. A separate one-dimensional Bayesian unfolding is used to correct the measured p_T^{jet} spectra that are used to normalize the unfolded $D(p_T, r)$ distributions, $1/A(r) \times d^2 n_{\text{ch}}^{\text{unfolded}} / dp_T dr$. This uses the same number of iterations as in the case of the two-dimensional unfolding. To achieve better correspondence with the data, the response matrices for both the one and two dimensional unfolding are reweighed so that the distributions match the shapes in the reconstructed data.

Finally, an independent bin-by-bin unfolding procedure is used to correct for biases originating from the finite jet and track angular resolutions. Two corresponding $D(p_T, r)$ distributions are evaluated in MC samples, one using generator-level jets and primary particles and the other using simulated jets and charged particles with their reconstructed p_T^{ch} replaced by generator-level transverse momentum, p_T^{truth} . The ratio of these two MC distributions provides a correction factor which is then applied to the data.

The performance of the full analysis procedure is validated in MC events where the entire correction procedure is performed using reconstructed jets and tracks, and the results are compared to the generator-level

distributions. These distributions agree with each other at the level of 4-5%.

6 Systematic uncertainties

The following sources of systematic uncertainty are considered: the jet energy scale (JES), the jet energy resolution (JER), the sensitivity of the unfolding to the prior, the UE contribution, the residual non-closure of the analysis procedure, and tracking-related uncertainties. For each systematic variation, the $D(p_T, r)$ distributions and their ratios are re-evaluated. The difference between the varied and nominal distributions is used as an estimate of the uncertainty.

The systematic uncertainty due to the JES in Pb+Pb collisions is composed of two parts: a centrality-independent baseline component and a centrality-dependent component. Only the centrality-independent baseline component is used in pp collisions; it is determined from *in-situ* studies of the calorimeter response [37–39] and the relative energy scale difference between the jet reconstruction procedure in heavy-ion collisions [38] and the procedure used in pp collisions [40]. The centrality-dependent uncertainty reflects a modification of parton showers by the Pb+Pb environment. It is evaluated by comparing calorimeter p_T^{jet} and the sum of p_T of tracks within the jet in data and MC. The size of the centrality-dependent uncertainty on the JES reaches 0.5% in the most central collisions. Each component that contributes to the JES uncertainty is varied separately by ± 1 standard deviation for each interval in p_T^{jet} and the response matrix is recomputed accordingly. The data are unfolded with modified matrices. The resulting uncertainty from the JES increases with increasing charged-particle p_T at fixed p_T^{jet} and decreases with increasing p_T^{jet} , and is at the level of 2–4%.

The uncertainty on the $D(p_T, r)$ distributions due to the JER is evaluated by repeating the unfolding procedure with modified response matrices, where an additional contribution is added to the resolution of the reconstructed p_T^{jet} using a Gaussian smearing procedure. The smearing factor is evaluated using an *in-situ* technique in 13 TeV pp data involving studies of dijet energy balance [41, 42]. An additional uncertainty is included to account for differences between the tower-based jet reconstruction and that used in analyses of 13 TeV pp data. The resulting uncertainty from the JER is symmetrized to account for negative variations of the JER. The size of the resulting uncertainty on the $D(p_T, r)$ distributions due to the JER typically reaches 4–5% for the highest charged-particle p_T intervals and decreases to 2–3% with decreasing charged-particle p_T at fixed p_T^{jet} .

The systematic uncertainty on the unfolding procedure is estimated by generating the response matrices from the MC distributions without any re-weighting to match shapes in data. Conservatively, the difference between the nominal $D(p_T, r)$ distribution and $D(p_T, r)$ unfolded with the re-weighted response matrices is taken as the systematic uncertainty, and is at the level of 5–7%.

The systematic uncertainty associated with the UE subtraction has two components: the statistical uncertainty on the charged particle distributions estimated in the MC overlay, and the comparison to the cone method (described in detail in Ref. [13]). The default method is limited by the finite statistics of the minimum bias data collected and the cone method is sensitive to hard scattering induced biases in the UE. The UE estimate from the default method requires centrality reweighting, whereas the estimate from the cone method matches the centrality distribution of the jet sample by construction. The UE uncertainty on the $D(p_T, r)$ distributions is approximately 40% at the largest distances from the jet axis and rapidly decreases with increasing charged-particle p_T and decreasing distance. This is the dominant source of the systematic uncertainty at low charged-particle p_T and large r .

The uncertainties related to track reconstruction and selection originate from several sources. Uncertainties related to the material description in simulation and the track transverse momentum resolution are obtained from studies in data and simulation described in Ref. [43]. The systematic uncertainty in the fake track rate is 30% in both collision systems [43]. The contamination of fake tracks is less than 2% and the resulting uncertainty in the $D(p_T, r)$ distributions is at most 5%. The sensitivity of the tracking efficiency to the description of the inactive material in the MC samples is evaluated by varying the material description. This resulting uncertainty in the track reconstruction efficiency is between 0.5% and 2% in the track p_T range used in the analysis. An additional uncertainty takes into account a possible residual misalignment of the tracking detectors in pp and Pb+Pb data-taking. The alignment in these datasets is checked *in-situ* with $Z \rightarrow \mu^+ \mu^-$ events, and thus a track- p_T dependent uncertainty arises from the finite size of this sample. The resulting uncertainties in the $D(p_T, r)$ distributions are typically less than 0.1%. An additional uncertainty in the tracking efficiency due to the high local track density in the core of jets is 0.4% [44] for all p_T^{jet} ranges in this analysis. The uncertainty due to the track selection is evaluated by repeating the analysis with an additional requirement on the significance of the distance of closest approach of the track to the primary vertex. This uncertainty affects the track reconstruction efficiencies, track momentum resolution, and rate of fake tracks. The resulting uncertainty typically varies between 1–2%. Finally, the track-to-particle association requirements are varied. This variation affects the track reconstruction efficiency, track momentum resolution, and rate of fake tracks. The resulting systematic uncertainty is $\leq 0.1\%$ on the $D(p_T, r)$ distributions. All track-related systematic uncertainties are added in quadrature and presented as total tracking uncertainty.

Conservatively, an additional uncertainty to account for possible residual limitations in the analysis procedure is assigned by evaluating the non-closure of the unfolded distributions in simulations, as described in Section 5.

Examples of systematic uncertainties in the $D(p_T, r)$ distributions for jets in the 126–158 GeV p_T^{jet} range measured in pp and Pb+Pb collision systems are shown in Figure 2. The uncertainties on the $R_{D(p_T, r)}$ and $\Delta D(p_T, r)$ distributions are shown in Figure 3 and Figure 4 respectively.

The correlations between the various systematic components are considered in evaluating the $R_{D(p_T, r)}$ and $\Delta D(p_T, r)$ distributions. The unfolding and non-closure uncertainty are taken to be uncorrelated between pp and Pb+Pb collisions and are combined as per the standard error propagation techniques:

$$\delta R_{D(p_T, r)} = R_{D(p_T, r)} \sqrt{\left(\frac{\delta D(p_T, r)_{\text{Pb+Pb}}}{D(p_T, r)_{\text{Pb+Pb}}} \right)^2 + \left(\frac{\delta D(p_T, r)_{pp}}{D(p_T, r)_{pp}} \right)^2} \quad (6)$$

$$\delta \Delta D(p_T, r) = \sqrt{\left(\delta D(p_T, r)_{\text{Pb+Pb}} \right)^2 + \left(\delta D(p_T, r)_{pp} \right)^2} \quad (7)$$

All other uncertainties are taken to be correlated. For these, the $R_{D(p_T, r)}$ and $\Delta D(p_T, r)$ distributions are re-evaluated by applying the variation to both collision systems; the resulting variations of the ratios from their central values are used as the correlated systematic uncertainty.

7 Results

The $D(p_T, r)$ distributions are studied as a function of p_T^{jet} for pp data and Pb+Pb collisions with different centralities. Ratios and differences between $D(p_T, r)$ distributions in Pb+Pb and pp collisions are evaluated to explore the impact of hot and dense matter on the parton shower.

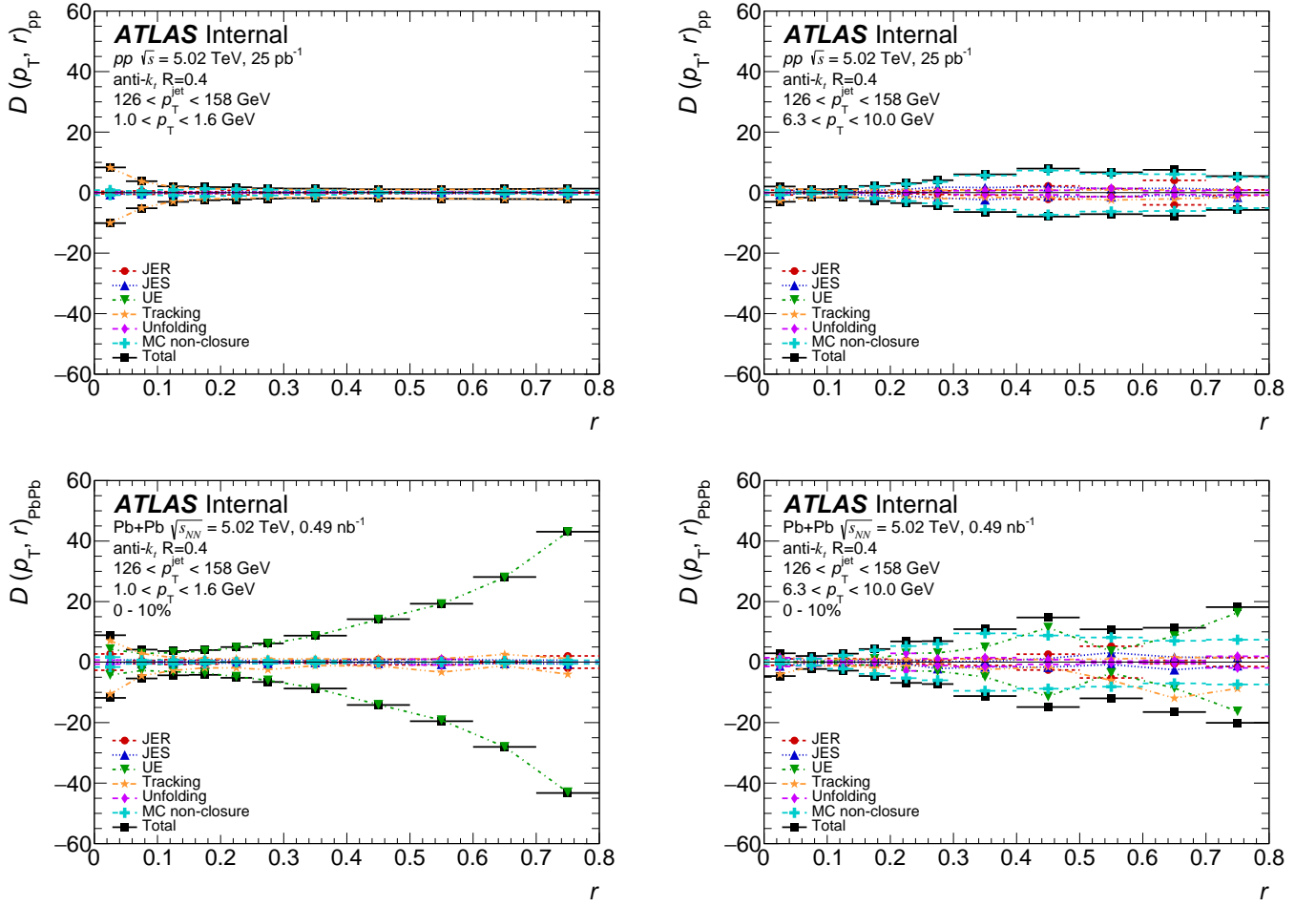


Figure 2: Relative size of the systematic uncertainties for $D(p_T, r)$ distributions in pp (top) and central (0-10%) Pb+Pb (bottom) collisions for tracks in the p_T range 1.0–1.6 GeV (left) and 6.3–10.0 GeV (right), in jets with $126 < p_T^{\text{jet}} < 158$ GeV. The systematic uncertainties due to JES, JER, unfolding, UE contribution, MC non-closure and tracking are shown along with the total systematic uncertainty from all sources.

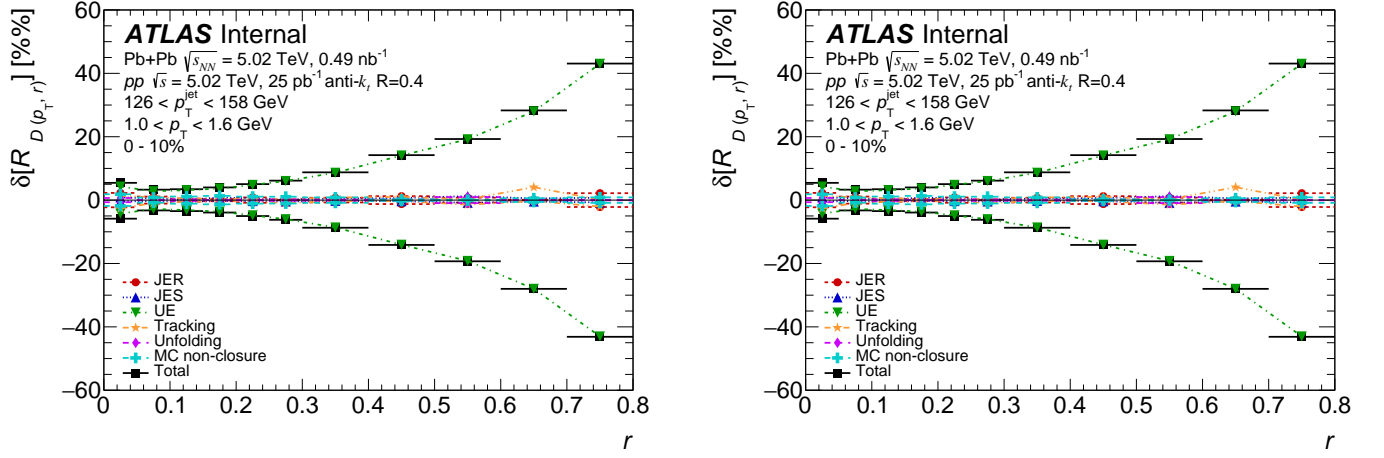


Figure 3: Relative size of the systematic uncertainties for $R_{D(p_T, r)}$ distributions for 0-10% Pb+Pb collisions, for tracks in the p_T range 1.0–1.6 GeV (left) and 6.3–10.0 GeV (right), in jets with $126 < p_T^{\text{jet}} < 158$ GeV. The systematic uncertainties due to JES, JER, unfolding, UE contribution, MC non-closure and tracking are shown along with the total systematic uncertainty from all sources.

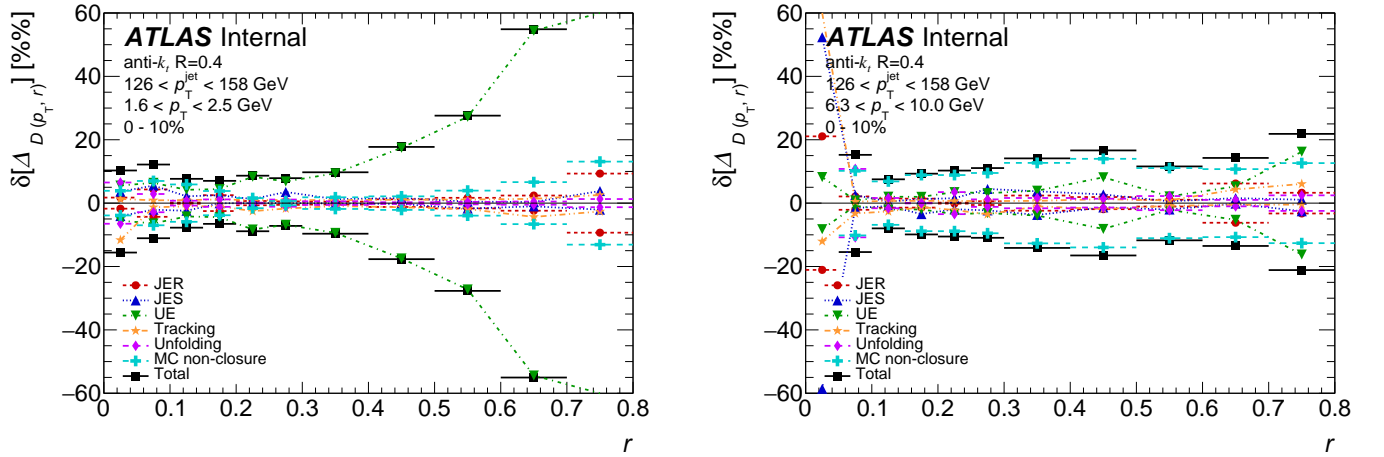


Figure 4: Relative size of the systematic uncertainties for $\Delta\Delta(p_T, r)$ distributions for 0-10% Pb+Pb collisions, for tracks in the p_T range 1.0–1.6 GeV (left) and 6.3–10.0 GeV (right), in jets with $126 < p_T^{\text{jet}} < 158$ GeV. The systematic uncertainties due to JES, JER, unfolding, UE contribution, MC non-closure and tracking are shown along with the total systematic uncertainty from all sources.

The $D(p_T, r)$ distributions evaluated in pp collisions, and in 0–10% and 60–80% Pb+Pb collisions, are shown in Figure 5. The distributions exhibit a difference in shape between central Pb+Pb collisions and the pp reference. On the contrary, the $D(p_T, r)$ distributions for peripheral Pb+Pb collisions are similar in shape to the pp reference.

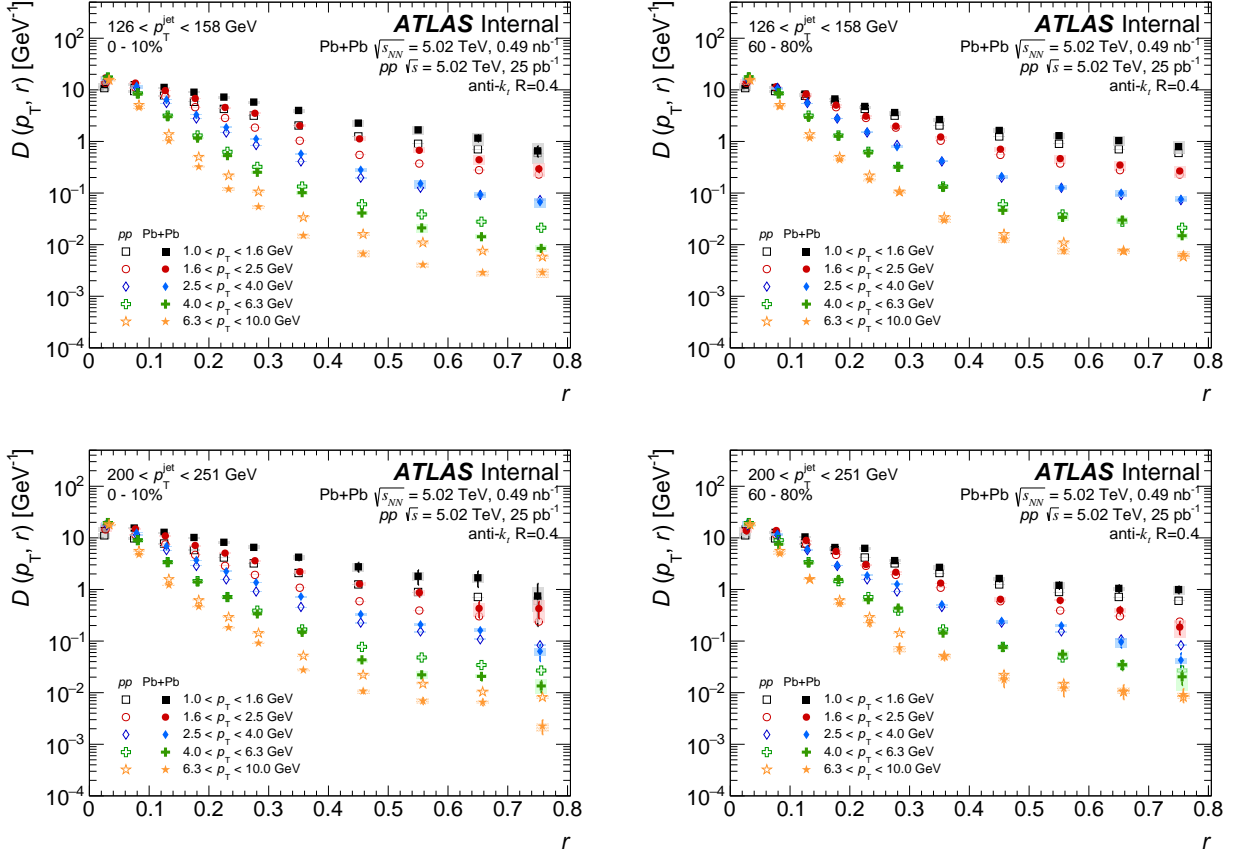


Figure 5: Closed symbols show $D(p_T, r)$ distributions in 0–10% (left) and 60–80% (right) Pb+Pb as a function of angular distance r for p_T^{jet} of 126 to 158 GeV (top) and of 200 to 251 GeV (bottom) for four p_T selections. Open symbols show $D(p_T, r)$ distributions in pp collisions. The vertical bars on the data points indicate statistical uncertainties while the shaded boxes indicate systematic uncertainties. There are no uncertainties on the r values, the finite widths of the shaded boxes are purely aesthetic.

Ratios of the $D(p_T, r)$ distributions in Pb+Pb to those measured in pp are presented in Figure 6 as a function of r for different p_T selections. In 0–10% central collisions, $R_{D(p_T, r)}$ is above unity at all r for charged-particles with p_T less than 4 GeV. For these particles, $R_{D(p_T, r)}$ grows with increasing r for $r < 0.3$ is approximately constant for $0.3 < r < 0.6$, and decreases for $0.6 < r < 0.8$. For $p_T > 4.0$ GeV, $R_{D(p_T, r)}$ is below unity and decreases with increasing r for $r < 0.3$ and is approximately constant for $0.3 < r < 0.8$. The observed behavior inside the jet ($r < 0.4$) agrees with the measurement of the inclusive jet fragmentation functions [8, 45], where yields of the low- p_T fragments are observed to be enhanced and yields of charged particles with intermediate p_T are suppressed in Pb+Pb collisions compared to those in pp collisions. For peripheral collisions, $R_{D(p_T, r)}$ has no significant r dependence and the distributions do not significantly deviate from unity. The measured dependence of $R_{D(p_T, r)}$ suggests that the energy lost by jets through the jet quenching process is being transferred to particles with $p_T < 4.0$ GeV with larger radial

distances. This is qualitatively consistent with theoretical calculations [16, 17].

The centrality dependence of $R_{D(p_T, r)}$ is presented in Figure 7 where the $R_{D(p_T, r)}$ for two p_T selections: 1.6–2.5 GeV and 6.3–10.0 GeV, and all centrality intervals are shown. The magnitude of these modifications decreases for more peripheral collisions and $R_{D(p_T, r)}$ goes towards unity in 60–80% central collisions for both p_T ranges, across the entire $r < 0.8$ range under investigation. This observation is in agreement with previous measurements of jet fragmentation functions [12, 13, 15, 45].

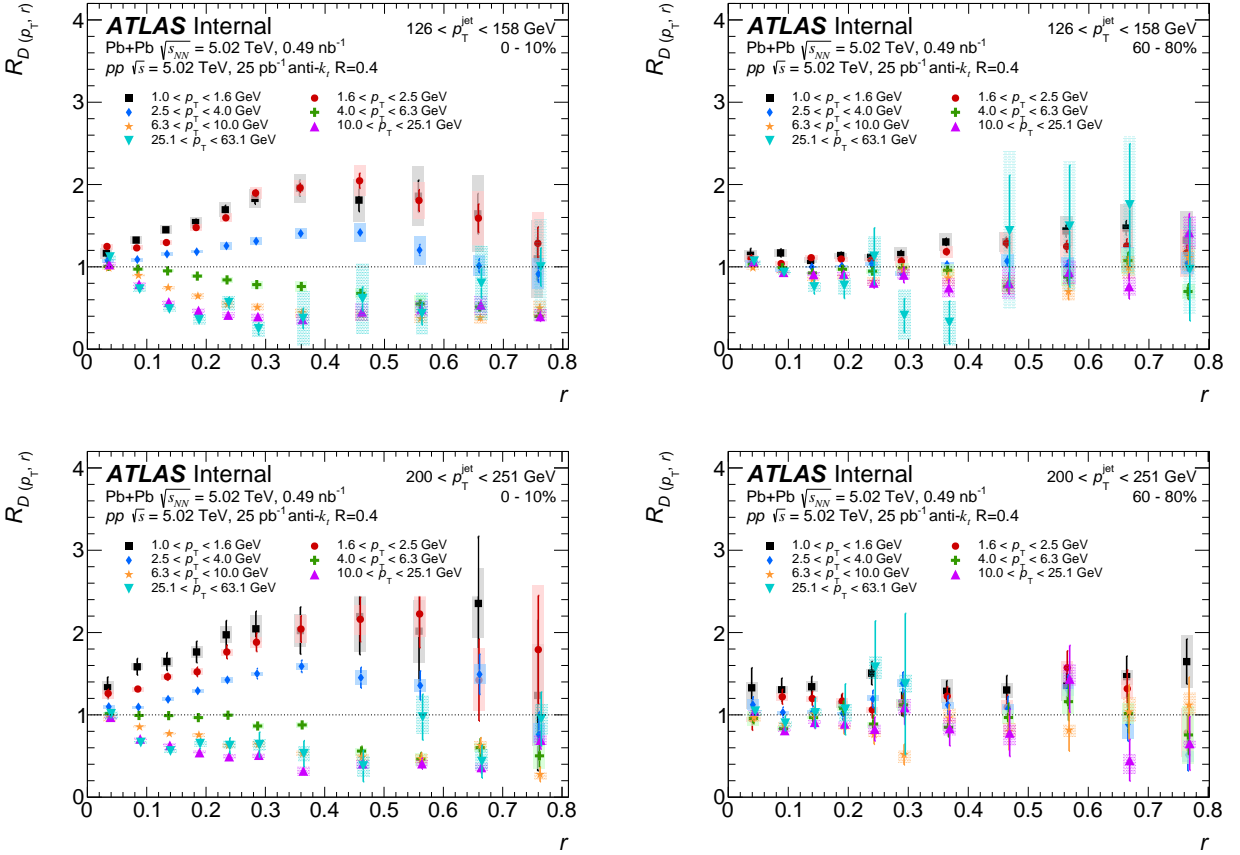


Figure 6: Ratios of $D(p_T, r)$ distributions in 0–10% (left) and 60–80% (right) Pb+Pb collisions to pp collisions as a function of angular distance r for p_T^{jet} of 126 to 158 GeV (top) and of 200 to 251 GeV (bottom) for six p_T selections. The vertical bars on the data points indicate statistical uncertainties while the shaded boxes indicate systematic uncertainties. There are no uncertainties on the r values, the finite widths of the shaded boxes are purely aesthetic.

The p_T^{jet} dependence of $R_{D(p_T, r)}$ in 0–10% central collisions is presented in Figure 8 where the $R_{D(p_T, r)}$ for two p_T selections: 1.0–1.6 GeV and 6.3–10.0 GeV, and four p_T^{jet} selections is shown. A statistically significant trend of increasing $R_{D(p_T, r)}$ with increasing p_T^{jet} is observed for $0.1 < r < 0.25$ for low p_T particles. This observation is in agreement with the previous measurement of jet fragmentation functions [12, 13, 15, 45] and may indicate the dependence of the response of the hot dense matter to the momentum of a jet passing through it. The higher- p_T charged particles have $R_{D(p_T, r)}$ values that decrease with increasing r ; no significant dependence on p_T^{jet} is observed.

The p_T^{ch} dependence of $R_{D(p_T, r)}$ in 0–10% central and 60–80% peripheral collisions is presented in Figure 9 where the $R_{D(p_T, r)}$ at different distances from the jet axis: $0.00 < r < 0.05$, $0.15 < r < 0.20$,

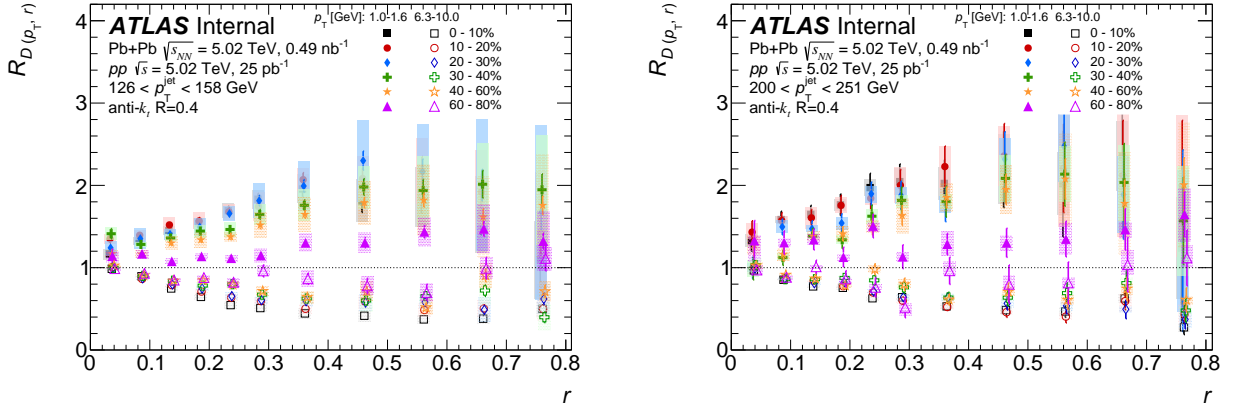


Figure 7: Ratios of $D(p_T, r)$ distributions for p_T^{jet} of 126 to 158 GeV (left) and of 200 to 251 GeV (right) in Pb+Pb collisions to pp collisions as a function of angular distance r for two p_T selections and six centrality intervals (p_T selections are shown by closed and open symbols). The vertical bars on the data points indicate statistical uncertainties while the shaded boxes indicate systematic uncertainties. There are no uncertainties on the r values, the finite widths of the shaded boxes are purely aesthetic.

0.30 < r < 0.40, 0.50 < r < 0.60, for 126 < p_T^{jet} < 158 GeV and 200 < p_T^{jet} < 251 GeV is shown. It can be seen that there is an enhancement in the number of particles in the jet core for all p_T , and that the depletion only happens for $r > 0.05$. The enhancement is larger for higher p_T^{jet} , and persists even for peripheral collisions. This observation is also in agreement with the previous measurement of jet fragmentation functions [12, 13, 15, 45]

Differences between the $D(p_T, r)$ distributions in Pb+Pb and pp are presented in Figure 10 as a function of r for different p_T selections. In 0–10% central collisions. These distributions indicate an excess (depletion) in the number of particles in the Pb+Pb system compared to the pp system for low (high) p_T particles. This excess ranges from 0.5 to 4 particles for 1 GeV tracks while the depletion ranges from ~0 to 0.5 particles for 10 GeV tracks. An increase in the extra number of particles with increasing p_T^{jet} for low p_T tracks is also seen.

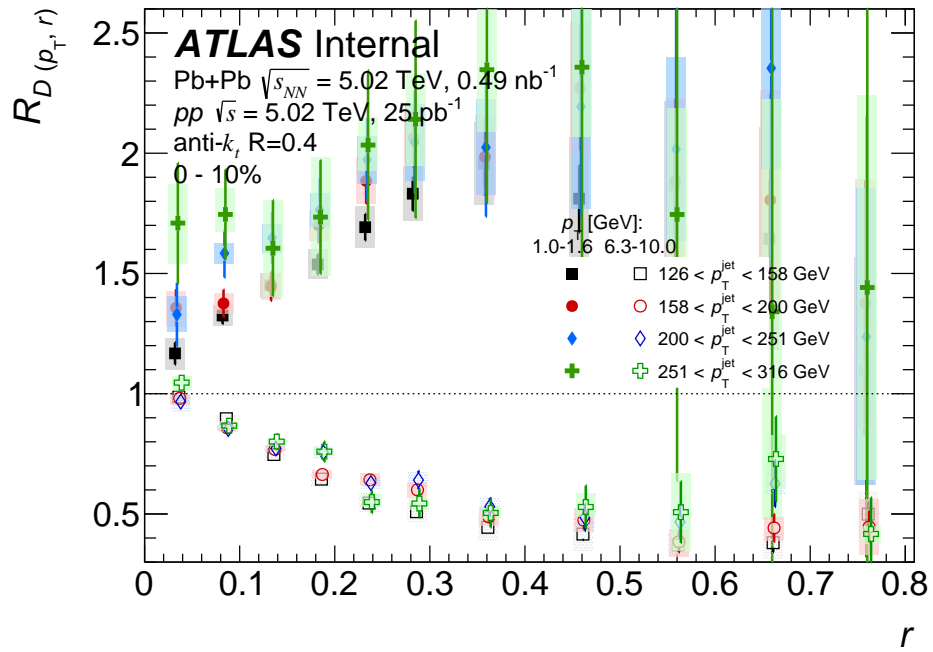


Figure 8: $R_{D(p_T, r)}$ as a function of r for 0–10% collisions for charged particles with $1.6 < p_T < 2.5$ GeV (closed symbols) and $6.3 < p_T < 10.0$ GeV (open symbols) for four p_T^{jet} selections: 126–158 GeV, 158–200 GeV, 200–251 GeV, and 251–316 GeV. There are no uncertainties on the r values, the finite widths of the shaded boxes are purely aesthetic.

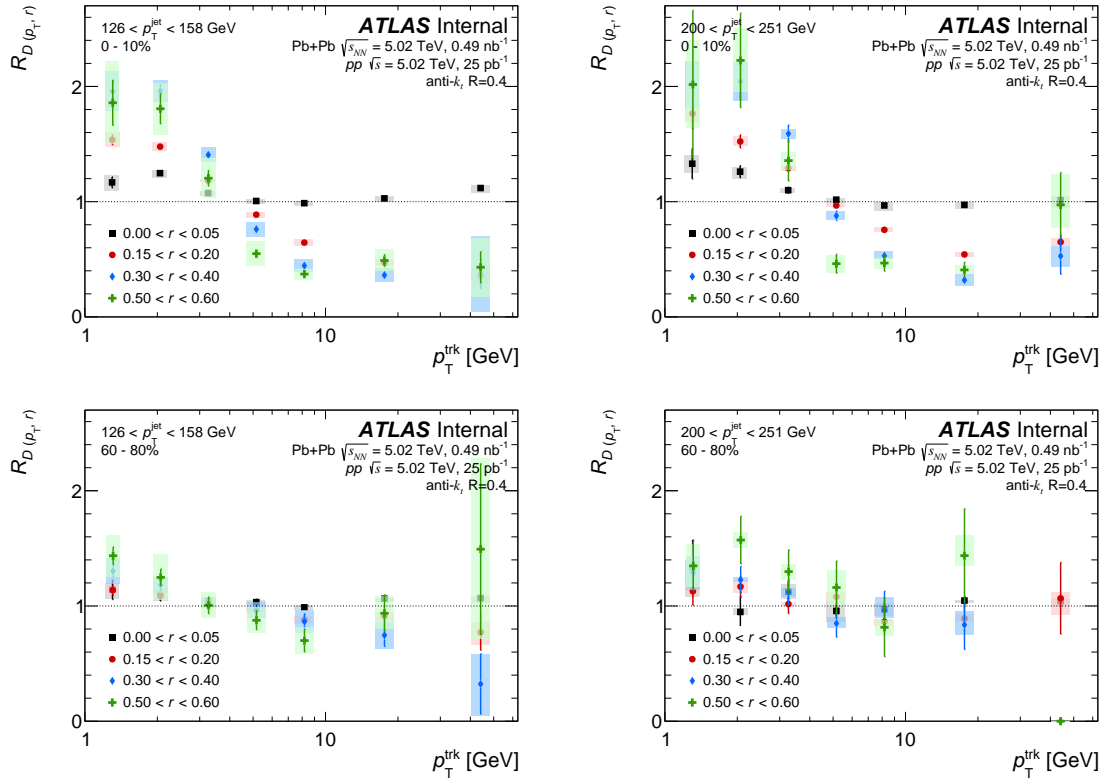


Figure 9: $R_D(p_T, r)$ as a function of p_T in central (top) and peripheral (bottom) collisions for two different p_T^{jet} selections: 126–158 GeV (left) and 200–251 GeV (right). The different colors indicate different distances from the jet axis

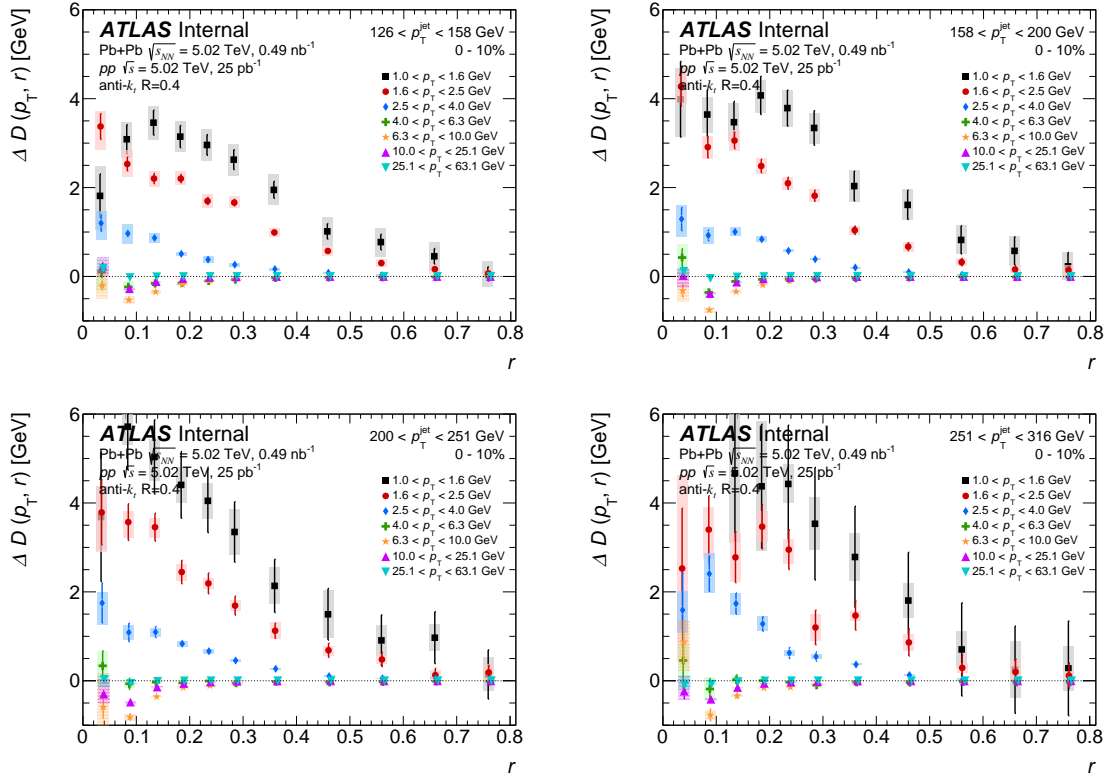


Figure 10: $\Delta R_{D(p_T, r)}$ as a function of r in central collisions for all p_T ranges in four p_T^{jet} selections: 126–158 GeV, 158–200 GeV, 200–251 GeV, and 251–316 GeV.

8 Summary

This note presents a measurement of the yields of charged particle distributions, $D(p_T, r)$ inside and around $R = 0.4$ anti- k_t jets with $|y^{\text{jet}}| < 1.7$, up to a distance of $R = 0.8$ from the jet axis. The yields are measured for p_T^{jet} from 126 to 316 GeV in Pb+Pb and pp collisions at 5.02 TeV as a function of charged particle p_T and the angular distance r between the jet axis and charged particle.

Centrality dependent modifications to the yields, when compared to those measured in pp collisions, are observed. The magnitude of these modifications increases with increasing collision centrality. The $R_{D(p_T, r)}$ distributions for charged particles with $p_T < 4$ GeV are above unity and grow with increasing angular separation up to $r \sim 0.3$, showing weak to no dependence on r in the interval $0.3 < r < 0.6$ followed with a small decrease in the enhancement between $0.6 < r < 0.8$. For charged particles with $p_T > 4$ GeV, a suppression in $R_{D(p_T, r)}$ is observed, and the distributions decrease with increasing r for $r < 0.3$, with no r dependence for $r > 0.3$. These results show a hint of broadening of the $D(p_T, r)$ distribution for low p_T particles inside the jet in central Pb+Pb collisions compared to those in pp collisions while for higher p_T particles angular distributions are narrower in Pb+Pb collisions compared to pp collisions. For all charged-particle p_T values the $R_{D(p_T, r)}$ values are greater than or equal to unity for small r values (inside the core of the jet). Between $0.1 < r < 0.25$, a statistically significant trend of increasing $R_{D(p_T, r)}$ with increasing p_T^{jet} is observed for low- p_T particles. No significant p_T^{jet} dependence is seen for particles with $p_T > 4$ GeV.

These measurements provide more information on the differential distributions of charged particles within jets as compared to the inclusive measurement of jet fragmentation functions. They may improve our understanding of the physics of soft gluon radiation and the response of the QGP to jets.

Acknowledgements

We thank CERN for the very successful operation of the LHC, as well as the support staff from our institutions without whom ATLAS could not be operated efficiently.

We acknowledge the support of ANPCyT, Argentina; YerPhI, Armenia; ARC, Australia; BMWFW and FWF, Austria; ANAS, Azerbaijan; SSTC, Belarus; CNPq and FAPESP, Brazil; NSERC, NRC and CFI, Canada; CERN; CONICYT, Chile; CAS, MOST and NSFC, China; COLCIENCIAS, Colombia; MSMT CR, MPO CR and VSC CR, Czech Republic; DNRF and DNSRC, Denmark; IN2P3-CNRS, CEA-DRF/IRFU, France; SRNSFG, Georgia; BMBF, HGF, and MPG, Germany; GSRT, Greece; RGC, Hong Kong SAR, China; ISF and Benoziyo Center, Israel; INFN, Italy; MEXT and JSPS, Japan; CNRST, Morocco; NWO, Netherlands; RCN, Norway; MNiSW and NCN, Poland; FCT, Portugal; MNE/IFA, Romania; MES of Russia and NRC KI, Russian Federation; JINR; MESTD, Serbia; MSSR, Slovakia; ARRS and MIZŠ, Slovenia; DST/NRF, South Africa; MINECO, Spain; SRC and Wallenberg Foundation, Sweden; SERI, SNSF and Cantons of Bern and Geneva, Switzerland; MOST, Taiwan; TAEK, Turkey; STFC, United Kingdom; DOE and NSF, United States of America. In addition, individual groups and members have received support from BCKDF, CANARIE, CRC and Compute Canada, Canada; COST, ERC, ERDF, Horizon 2020, and Marie Skłodowska-Curie Actions, European Union; Investissements d'Avenir Labex and Idex, ANR, France; DFG and AvH Foundation, Germany; Herakleitos, Thales and Aristeia programmes co-financed by EU-ESF and the Greek NSRF, Greece; BSF-NSF and GIF, Israel;

406 CERCA Programme Generalitat de Catalunya, Spain; The Royal Society and Leverhulme Trust, United
407 Kingdom.

408 The crucial computing support from all WLCG partners is acknowledged gratefully, in particular from
409 CERN, the ATLAS Tier-1 facilities at TRIUMF (Canada), NDGF (Denmark, Norway, Sweden), CC-IN2P3
410 (France), KIT/GridKA (Germany), INFN-CNAF (Italy), NL-T1 (Netherlands), PIC (Spain), ASGC
411 (Taiwan), RAL (UK) and BNL (USA), the Tier-2 facilities worldwide and large non-WLCG resource
412 providers. Major contributors of computing resources are listed in Ref. [\[46\]](#).

Appendix

In a paper, an appendix is used for technical details that would otherwise disturb the flow of the paper. Such an appendix should be printed before the Bibliography.

References

- [1] G. Roland, K. Šafařík and P. Steinberg, *Heavy-ion collisions at the LHC*, *Prog. Part. Nucl. Phys.* **77** (2014) 70 (cit. on p. 2).
- [2] W. Busza, K. Rajagopal and W. van der Schee, *Heavy Ion Collisions: The Big Picture, and the Big Questions*, (2018), arXiv: [1802.04801 \[hep-ph\]](#) (cit. on p. 2).
- [3] ALICE Collaboration, *Measurement of charged jet suppression in Pb-Pb collisions at $\sqrt{s_{NN}} = 2.76$ TeV*, *JHEP* **03** (2014) 013, arXiv: [1311.0633 \[nucl-ex\]](#) (cit. on p. 2).
- [4] ATLAS Collaboration, *Measurements of the Nuclear Modification Factor for Jets in Pb+Pb Collisions at $\sqrt{s_{NN}} = 2.76$ TeV with the ATLAS Detector*, *Phys. Rev. Lett.* **114** (2015) 072302, arXiv: [1411.2357 \[hep-ex\]](#) (cit. on pp. 2, 4).
- [5] CMS Collaboration, *Measurement of inclusive jet cross sections in pp and PbPb collisions at $\sqrt{s_{NN}} = 2.76$ TeV*, *Phys. Rev. C* **96** (2017) 015202, arXiv: [1609.05383 \[nucl-ex\]](#) (cit. on p. 2).
- [6] ATLAS Collaboration, *Observation of a Centrality-Dependent Dijet Asymmetry in Lead-Lead Collisions at $\sqrt{s_{NN}} = 2.76$ TeV with the ATLAS Detector at the LHC*, *Phys. Rev. Lett.* **105** (2010) 252303, arXiv: [1011.6182 \[hep-ex\]](#) (cit. on p. 2).
- [7] CMS Collaboration, *Observation and studies of jet quenching in PbPb collisions at nucleon-nucleon center-of-mass energy = 2.76 TeV*, *Phys. Rev. C* **84** (2011) 024906, arXiv: [1102.1957 \[nucl-ex\]](#) (cit. on p. 2).
- [8] ATLAS Collaboration, *Measurement of jet p_T correlations in Pb+Pb and pp collisions at $\sqrt{s_{NN}} = 2.76$ TeV with the ATLAS detector*, *Phys. Lett. B* **774** (2017) 379, arXiv: [1706.09363 \[hep-ex\]](#) (cit. on pp. 2, 10).
- [9] CMS Collaboration, *Studies of jet quenching using isolated-photon+jet correlations in PbPb and pp collisions at $\sqrt{s_{NN}} = 2.76$ TeV*, *Phys. Lett. B* **718** (2013) 773, arXiv: [1205.0206 \[nucl-ex\]](#) (cit. on p. 2).
- [10] CMS Collaboration, *Modification of jet shapes in PbPb collisions at $\sqrt{s_{NN}} = 2.76$ TeV*, *Phys. Lett. B* **730** (2014) 243, arXiv: [1310.0878 \[nucl-ex\]](#) (cit. on p. 2).
- [11] ATLAS Collaboration, *Measurement of inclusive jet charged-particle fragmentation functions in Pb+Pb collisions at $\sqrt{s_{NN}} = 2.76$ TeV with the ATLAS detector*, *Phys. Lett. B* **739** (2014) 320, arXiv: [1406.2979 \[hep-ex\]](#) (cit. on p. 2).
- [12] CMS Collaboration, *Measurement of jet fragmentation in PbPb and pp collisions at $\sqrt{s_{NN}} = 2.76$ TeV*, *Phys. Rev. C* **90** (2014) 024908, arXiv: [1406.0932 \[nucl-ex\]](#) (cit. on pp. 2, 13, 14).
- [13] ATLAS Collaboration, *Measurement of jet fragmentation in Pb+Pb and pp collisions at $\sqrt{s_{NN}} = 2.76$ TeV with the ATLAS detector at the LHC*, *Eur. Phys. J. C* **77** (2017) 379, arXiv: [1702.00674 \[hep-ex\]](#) (cit. on pp. 2, 9, 13, 14).

- [14] CMS Collaboration, *Decomposing transverse momentum balance contributions for quenched jets in PbPb collisions at $\sqrt{s_{NN}} = 2.76$ TeV*, *JHEP* **11** (2016) 055, arXiv: [1609.02466 \[nucl-ex\]](#) (cit. on p. 2).
- [15] A. M. Sirunyan et al., *Jet properties in PbPb and pp collisions at $\sqrt{s_{NN}} = 5.02$ TeV*, (2018), arXiv: [1803.00042 \[nucl-ex\]](#) (cit. on pp. 2, 13, 14).
- [16] G.-Y. Qin and X.-N. Wang, *Jet quenching in high-energy heavy-ion collisions*, *Int. J. Mod. Phys. E* **24** (2015) 1530014 (cit. on pp. 2, 13).
- [17] J.-P. Blaizot, Y. Mehtar-Tani and M. A. C. Torres, *Angular structure of the in-medium QCD cascade*, *Phys. Rev. Lett.* **114** (2015) 222002, arXiv: [1407.0326 \[hep-ph\]](#) (cit. on pp. 2, 13).
- [18] M. Cacciari, G. P. Salam and G. Soyez, *The Anti- $k(t)$ jet clustering algorithm*, *JHEP* **0804** (2008) 063, arXiv: [0802.1189 \[hep-ph\]](#) (cit. on p. 3).
- [19] ATLAS Collaboration, *The ATLAS Experiment at the CERN Large Hadron Collider*, *JINST* **3** (2008) S08003 (cit. on p. 3).
- [20] ATLAS Collaboration, *ATLAS Insertable B-Layer Technical Design Report*, (2010), ATLAS-TDR-19, URL: <http://cds.cern.ch/record/1291633> (cit. on p. 3).
- [21] ATLAS Collaboration, *ATLAS Insertable B-Layer Technical Design Report Addendum*, (2012), ATLAS-TDR-19-ADD-1, URL: <http://cds.cern.ch/record/1451888> (cit. on p. 3).
- [22] P. Nason, *A New method for combining NLO QCD with shower Monte Carlo algorithms*, *JHEP* **11** (2004) 040, arXiv: [hep-ph/0409146 \[hep-ph\]](#) (cit. on p. 4).
- [23] T. Sjöstrand et al., *An Introduction to PYTHIA 8.2*, *Comput. Phys. Commun.* **191** (2015) 159, arXiv: [1410.3012 \[hep-ph\]](#) (cit. on p. 4).
- [24] ATLAS Collaboration, *ATLAS Run 1 Pythia8 tunes*, (2014), ATLAS-PHYS-PUB-2014-021, URL: <https://cds.cern.ch/record/1966419> (cit. on p. 4).
- [25] R. D. Ball et al., *Parton distributions with LHC data*, *Nucl. Phys. B* **867** (2013) 244, arXiv: [1207.1303 \[hep-ph\]](#) (cit. on p. 4).
- [26] GEANT4 Collaboration, S. Agostinelli et al., *GEANT4: A simulation toolkit*, *Nucl. Instrum. Meth. A* **506** (2003) 250 (cit. on p. 4).
- [27] ATLAS Collaboration, *The ATLAS Simulation Infrastructure*, *Eur. Phys. J. C* **70** (2010) 823, arXiv: [1005.4568 \[physics.ins-det\]](#) (cit. on pp. 4, 5).
- [28] ATLAS Collaboration, *Measurement of longitudinal flow de-correlations in Pb+Pb collisions at $\sqrt{s_{NN}} = 2.76$ and 5.02 TeV with the ATLAS detector*, *Eur. Phys. J. C* **78** (2018) 142, arXiv: [1709.02301 \[nucl-ex\]](#) (cit. on p. 4).
- [29] ATLAS Collaboration, *Measurement of the azimuthal anisotropy for charged particle production in $\sqrt{s_{NN}} = 2.76$ TeV lead-lead collisions with the ATLAS detector*, *Phys. Rev. C* **86** (2012) 014907, arXiv: [1203.3087 \[hep-ex\]](#) (cit. on pp. 5, 6).
- [30] ATLAS Collaboration, *Jet energy scale measurements and their systematic uncertainties in proton-proton collisions at $\sqrt{s} = 13$ TeV with the ATLAS detector*, *Phys. Rev. D* **96** (2017) 072002, arXiv: [1703.09665 \[hep-ex\]](#) (cit. on p. 5).
- [31] ATLAS Collaboration, *Properties of jets and inputs to jet reconstruction and calibration with the ATLAS detector using proton-proton collisions at $\sqrt{s} = 13$ TeV*, ATL-PHYS-PUB-2015-036, 2015, URL: <https://cds.cern.ch/record/2044564> (cit. on p. 5).

- [32] ATLAS Collaboration, *Study of photon-jet momentum correlations in Pb+Pb and pp collisions at $\sqrt{s_{NN}} = 5.02$ TeV with ATLAS*, ATLAS-CONF-2016-110, 2016, URL: <https://cds.cern.ch/record/2220772> (cit. on p. 5).
- [33] ATLAS Collaboration, *Performance of the ATLAS Track Reconstruction Algorithms in Dense Environments in LHC Run 2*, *Eur. Phys. J. C* **77** (2017) 673, arXiv: 1704.07983 [hep-ex] (cit. on p. 5).
- [34] *Measurement of the azimuthal anisotropy of charged particles produced in 5.02 TeV Pb+Pb collisions with the ATLAS detector*, tech. rep. ATLAS-CONF-2016-105, CERN, 2016, URL: <https://cds.cern.ch/record/2220372> (cit. on p. 7).
- [35] G. D'Agostini, *A Multidimensional unfolding method based on Bayes' theorem*, *Nucl. Instrum. Meth. A* **362** (1995) 487 (cit. on p. 8).
- [36] T. Adye, *Unfolding algorithms and tests using RooUnfold*, *Proceedings of the PHYSTAT 2009 Workshop*, CERN, Geneva, Switzerland, CERN-2011-006, pp 313 (2011), arXiv: 1105.1160 [physics.data-an] (cit. on p. 8).
- [37] ATLAS Collaboration, *Jet energy measurement with the ATLAS detector in proton-proton collisions at $\sqrt{s} = 7$ TeV*, *Eur. Phys. J. C* **73** (2013) 2304, arXiv: 1112.6426 [hep-ex] (cit. on p. 8).
- [38] ATLAS Collaboration, *Jet energy scale and its uncertainty for jets reconstructed using the ATLAS heavy ion jet algorithm*, (2015), ATLAS-CONF-2015-016, URL: <https://cds.cern.ch/record/2008677> (cit. on p. 8).
- [39] ATLAS Collaboration, *Jet calibration and systematic uncertainties for jets reconstructed in the ATLAS detector at $\sqrt{s}=13$ TeV*, (2015), ATLAS-PHYS-PUB-2015-015, URL: <https://cds.cern.ch/record/2037613> (cit. on p. 8).
- [40] ATLAS Collaboration, *Jet energy measurement and its systematic uncertainty in proton-proton collisions at $\sqrt{s} = 7$ TeV with the ATLAS detector*, *Eur. Phys. J. C* **75** (2015) 17, arXiv: 1406.0076 [hep-ex] (cit. on p. 8).
- [41] ATLAS Collaboration, *Jet energy resolution in proton-proton collisions at $\sqrt{s} = 7$ TeV recorded in 2010 with the ATLAS detector*, *Eur. Phys. J. C* **73** (2013) 2306, arXiv: 1210.6210 [hep-ex] (cit. on p. 9).
- [42] ATLAS Collaboration, *Data-driven determination of the energy scale and resolution of jets reconstructed in the ATLAS calorimeters using dijet and multijet events at $\sqrt{s} = 8$ TeV*, (2015), ATLAS-CONF-2015-017, URL: <https://cds.cern.ch/record/2008678> (cit. on p. 9).
- [43] ATLAS Collaboration, *Early Inner Detector Tracking Performance in the 2015 Data at $\sqrt{s} = 13$ TeV*, ATL-PHYS-PUB-2015-051, 2015, URL: <https://cds.cern.ch/record/2110140> (cit. on p. 9).
- [44] ATLAS Collaboration, *Measurement of track reconstruction inefficiencies in the core of jets via pixel dE/dx with the ATLAS experiment using $\sqrt{s} = 13$ TeV pp collision data*, ATL-PHYS-PUB-2016-007, 2016, URL: <https://cds.cern.ch/record/2140460> (cit. on p. 9).
- [45] A. Collaboration, *Measurement of jet fragmentation in Pb+Pb and pp collisions at $\sqrt{s_{NN}} = 5.02$ TeV with the ATLAS detector*, *Phys. Rev. C* **98** (2 2018) 024908, URL: <https://link.aps.org/doi/10.1103/PhysRevC.98.024908> (cit. on pp. 10, 13, 14).
- [46] ATLAS Collaboration, *ATLAS Computing Acknowledgements*, ATL-GEN-PUB-2016-002, URL: <https://cds.cern.ch/record/2202407> (cit. on p. 19).

Auxiliary material

In an ATLAS paper, auxiliary plots and tables that are supposed to be made public should be collected in an appendix that has the title ‘Auxiliary material’. This information will appear on the public webpage, but will not be included in the document submitted to arXiv and to the journal.